Supporting Information: Decoupling ionic defect energetics and electronic alignment in mixed conducting oxides

Matthäus Siebenhofer, Claudia Steinbach, Georg Kresse, Jürgen Fleig

S.I.1: Defect concentrations in STO and LSF

The solid lines in Fig. 1 show equilibrium oxygen vacancy and electron hole concentrations for $SrTiO_3$ with 6 ppm Ti vacancies as acceptor doping (corresponding to nominally undoped $SrTiO_3$ single crystals) and for $La_{0.6}Sr_{0.4}FeO_{3-\delta}$, calculated from the charged oxygen vacancy formation energy and the charge neutrality condition, using a standard oxygen chemical potential at 600 °C[1]. Defect concentrations were calculated using a self-consistent charge-neutrality model based on the electronic density of states (DOS). The DOS was read on an energy grid referenced to the valence band edge. At a fixed temperature, the oxygen chemical potential was varied according to

$$\mu_O(T, p_{O_2}) = \frac{1}{2}\left[\mu^0_{O_2}(T) + k_B T \ln(p_{O_2})\right],$$

and, for each p_{O_2} (normalized to 1 bar), the Fermi level was determined by solving the charge-neutrality condition

$$p(E_F) + 2[V_O^{\bullet\bullet}](E_F, p_{O_2}) + q_{acc.} = 0.$$

Hole concentrations were obtained by numerical integration of the DOS weighted by the Fermi–Dirac occupation in the valence band. Oxygen vacancies were treated as charged defects on a finite oxygen-site reservoir, with a formation free energy

$$\Delta_r g_{V_O} = \Delta_r g^0 + 2E_F + \frac{1}{2} k_B T \ln(p_{O_2})$$

where $\Delta_r g^0$ corresponds to the calculated charged oxygen vacancy formation energy with the VBM as the electronic reservoir. The resulting self-consistent values of E_F, $[V_O^{\bullet\bullet}]$, and p were stored as functions of p_{O_2} and used to generate the Brouwer diagrams. For comparison, the dashed lines show oxygen vacancy concentrations and electron hole concentrations calculated from literature defect models at 600 °C[2,3].

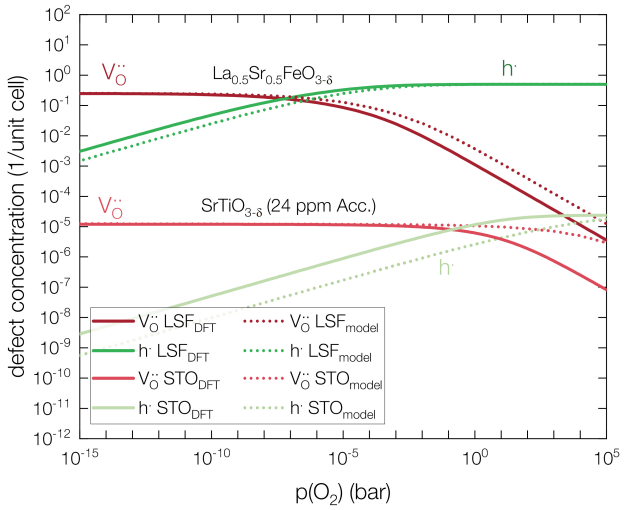

Figure 1. Defect concentrations in LSF and STO calculated both from defect models from literature as well as from reducibilities evaluated from DFT calculations. For STO, an acceptor concentration of 6 ppm Ti vacancies was assumed.

S.I.2: Space charges at STO|LSM and STO|LMO interfaces

As discussed in the main manuscript, materials with similar $\Delta_r g^0$ can produce strongly different responses in various applications, based on their electronic energy alignment. As an example, we show here measurements of the space charge resistance at the $SrTiO_{3-\delta}|La_{0.65}Sr_{0.35}MnO_{3-\delta}$ interface, compared with the $SrTiO_{3-\delta}|LiMn_2O_{4-\delta}$ interface. Both the perovskite oxide LSM, and the spinel oxide LMO contain Mn as the transition metal cation, and the formal oxidation state is 3.2 in LSM and 3.5 in LMO at stoichiometric oxygen content. Calculations of $La_{0.5}Sr_{0.5}MnO_{3-\delta}$ and $LiMn_2O_{4-\delta}$ yield high $\Delta_r g^0$ values of 3.6 eV for LSM and 2.4 eV for LMO (compared with 0.6 eV for STO). However, while the Fermi level of LSM lies around 2 eV above the STO VBM, the VBM of LMO lies 0.8 eV below the STO VBM. Therefore, it is expected that the two materials produce substantially different space charge zones, with LSM yielding a very high space charge potential (and therefore resistance). For LMO, we would in fact expect no electron hole depletion in STO at all, and possibly even an accumulation zone because of the low VBM (however, this would not be visible in the here discussed impedance measurements because of the comparatively large serial STO bulk resistance). Although the experimental LSM composition differs from the $La_{0.5}Sr_{0.5}MnO_3$ composition used in the computational map, both compositions have a high-lying Mn-derived electronic reservoir relative to STO, so the qualitative space-charge argument remains the same.

Fig. 2 shows the impedance response of the STO|LSM and the STO|LMO interface. The exact measurement methodology is detailed in our earlier work[4]. While the STO|LSM interface exhibits a large impedance feature with a resonance frequency close to 10 Hz, the STO|LMO interfacedoes not exhibit this feature. The small low frequency feature visible in the zoomed in figure represents the transition from mixed ionic electronic to purely electronic conduction in the STO single crystal[2] and is also visible in the STO|LSM measurement, however, it only occurs as a slight shoulder at the low frequency end of the large space charge feature. Small deviations in the STO conductivity may originate in acceptor dopant concentration variation between single crystals, or slight temperature or $p(O_2)$ differences. These measurements strongly support the conclusion that the two materials LSM and LMO produce extremely different space charge regions in STO because of the strongly different electronic energy alignment.

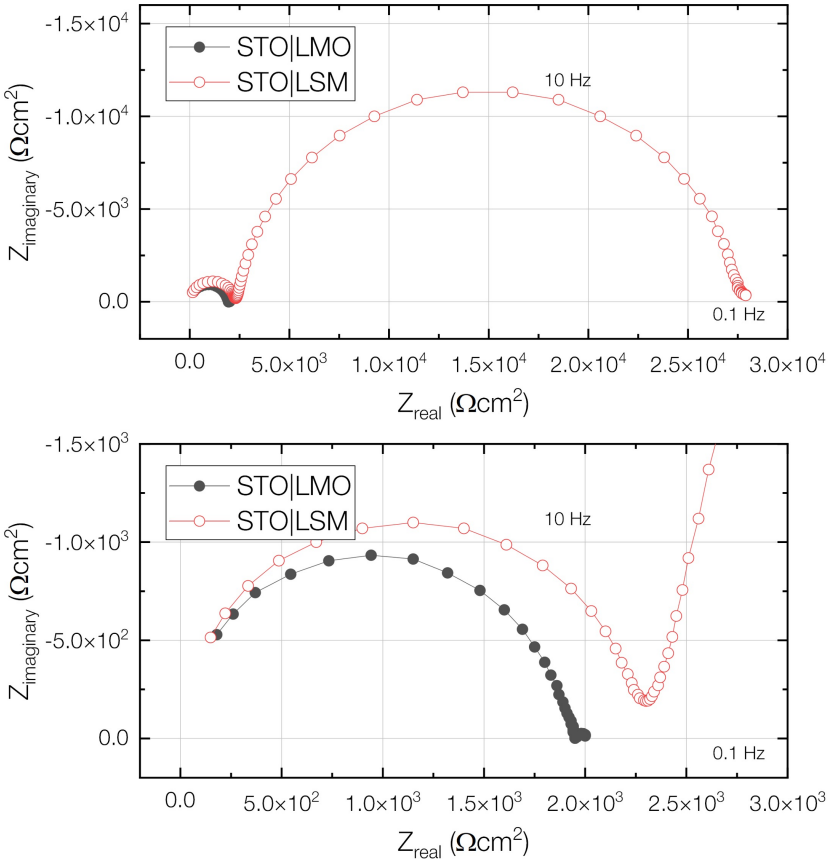

Figure 2. Impedance responses of the STO|LSM and the STO|LMO interfaces measured at 500 °C and 0.5 mbar $p(O_2)$.

S.I.3: Discussing the O 2p band center as a descriptor for oxide properties

The O 2p band center (the distance between the centroid of the O 2p states and the Fermi level) has been established as a powerful descriptor for catalyst performance[5–8] and as a proxy for the oxygen vacancy formation energy, especially for perovskite oxides[5,9,10]. Since the present analysis extends this space to fluorite and spinel oxides, we also test here the correlation between the O 2p band center and the charged oxygen vacancy formation energy.

Fig. 3 shows the variation of the charged oxygen vacancy formation energy with the O 2p band center referenced vs. the VBM or E_F (x-axis), and the alignment of the VBM or E_F vs. STO (via color coding). Within the present dataset, the O 2p band center (the distance between the centroid of the O 2p states and the VBM) is a reasonable first-order estimate of charged oxygen vacancy formation energies, with an r^2 of 0.84. There are, however, aspects that it is not able to capture:

- Subtle variations in the electronic structure, such as changes in metal-oxygen hybridization, as well as a changing filling of bonding and antibonding states. This is clearly seen in the large variation between perovskites with different B-site cations, STO, SMO, and SFO.
- The absolute position of the valence band. While the majority of the O 2p states (i.e. the nonbonding states) lie roughly at the same energy for the studied perovskite oxides, this changes entirely for other structures, such as fluorite or spinel oxides. This leads to interesting phenomena, such as the comparison between STO, ceria, and LMO. Although both ceria and LMO have a substantially deeper VBM than STO, one has a substantially lower and one a substantially higher vacancy formation energy. This can be easily explained by the absolute position of the O 2p states, which lie much deeper in LMO, indicating highly stable oxygen.

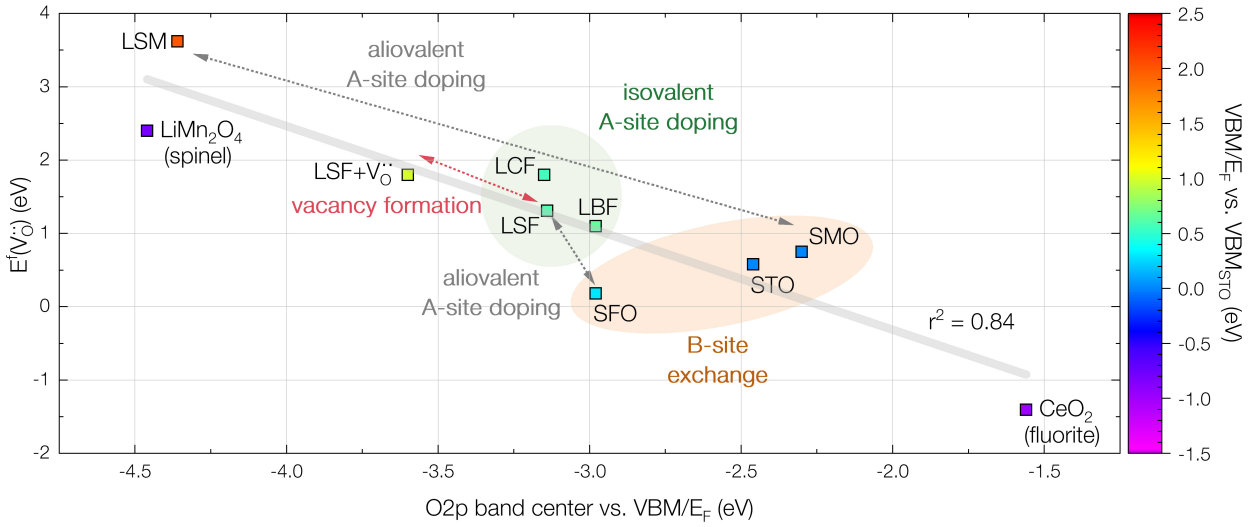

Figure 3. Map of the variation of $E^f(V_O^{\cdot\cdot}) = \Delta_r g^0$ with the O2$_p$ band center of all studied mixed conducting oxides. The color coding denotes the absolute position of the VBM (or E_F) with respect to the VBM of STO.

S.I.4: Relevance of $\mu_{h^\cdot}^0$ and $\mu_{V_O^{\cdot\cdot}}^0$ for application

Depending on the application, the decisive material parameters may either be reducibility and oxygen vacancy formation energies, or the individual components of electron redistribution and oxide ion removal treated as independent, separately tunable levers. We therefore group MIEC applications into three categories (visualized in Fig. 4) and summarize which energetic quantities are essential for each case.

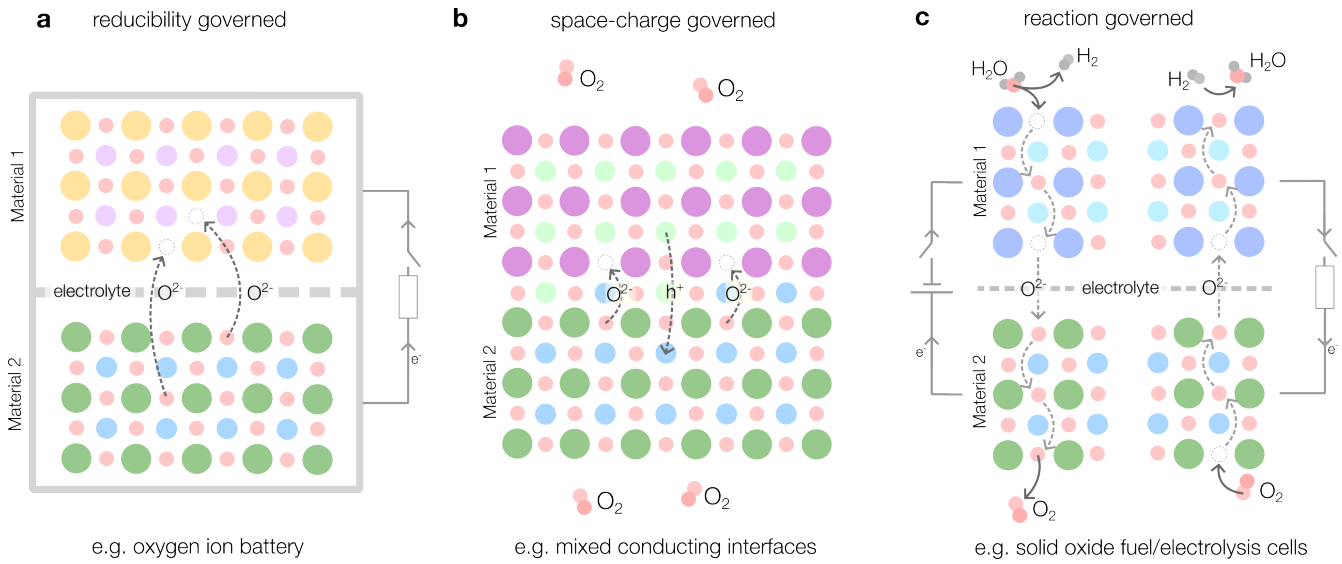

Figure 4. a) Schematic of a charged oxygen ion battery at open circuit as an example for a reducibility governed device. b) Schematic of an interface between two mixed conductors as an example for a space charge governed junction. c) Schematic of a solid oxide cell in open circuit conditions for fuel cell and electrolysis mode as an example for a reaction governed device.

Reducibility governed devices rely on the thermodynamics of oxygen vacancy formation, i.e. on $\Delta_r g^0 = \mu_O^0 + \mu_{V_O^{\cdot\cdot}}^0 - 2\mu_{h^\cdot}^0$. A prototypical example is an oxygen ion battery[11], a storage concept in which an oxygen chemical potential difference between two solids sets the attainable open-circuit voltage. Another example of reducibility-governed processes is solar-to-fuel conversion[12], where a material is reduced at high temperature, and the oxidation reaction at lower temperatures drives a chemical reaction, such as water splitting. Both driving forces for reduction and oxidation are governed by reducibility. In this category, the combination of electron redistribution and oxide ion removal matters most; different absolute values of $\mu_{V_O^{\cdot\cdot}}^0$ and $\mu_{h^\cdot}^0$ can therefore lead to similar net reducibility.

Space charge governed devices are controlled by absolute alignment of defect energies across interfaces. Here, the separate offsets $\Delta\mu_{h^\cdot}^0$ and $\Delta\mu_{V_O^{\cdot\cdot}}^0$ determine interfacial potentials, depletion/accumulation profiles, and thus junction resistances. This situation occurs at heterojunctions between two mixed conductors, at mixed conductor|electrolyte interfaces, and at internal junctions (e.g., grain boundaries[13,14]). In memristive devices, for example, space-charge formation in the mixed-conducting channel depends sensitively on alignment to the ionic conductor/electrolyte and can be either desirable if intentionally designed or detrimental, obscuring the mechanism of resistance modulation. Importantly, in this category, device behavior can change strongly with electronic alignment even at similar bulk reducibility (see comparison between LSM and LMO).

Reaction governed devices comprise most electrode and catalyst applications, including solid oxide fuel and electrolysis cells. Here, the rate is set by surface reaction kinetics, which typically involve charge-transfer steps and therefore depend on absolute electron energies (work function / band alignment) in addition to defect availability, which is controlled by reducibility. Recent work has shown that surface modifications can systematically tune the work function and accelerate oxygen exchange, consistent with an electronic-structure control of charge-transfer steps[15–17]. At the same time, oxygen vacancies and related lattice defects are often active participants in reaction pathways, so reducibility (and thus the balance of electron redistribution and oxide ion removal) remains an additional tuning knob[18]. In this category, optimal activity generally requires simultaneous control of energy alignment and defect thermodynamics.

S.I.5: Impact of interfacial termination

While the (110) oriented interface slabs avoid this problem, for perovskite (001) interface slabs, the choice of termination can affect the extracted band alignment through (i) changes in overall stoichiometry and (ii) an interfacial dipole. This is particularly relevant when interfacing nominally charge-neutral planes of a 2-4 perovskite (e.g., $SrTiO_3$) with polar planes of a 3-3 perovskite (e.g., $LaFeO_3$), where alternating layer charges can induce a net dipole depending on the A-site composition. To quantify this effect, we compared (001) STO|LSF slabs with two interfacial A-site compositions (100% Sr and 75% Sr) using the PBE functional. For 100% Sr the interfacial AO plane is STO like, while for 75% Sr, we expect a mixed, nearly dipole-free situation. The VBM offset changes from 0.25 eV (100% Sr) to 0.45 eV (75% Sr), indicating that termination/stoichiometry-related dipole effects shift the alignment by roughly 0.2 eV.

Because these PBE offsets differ from the HSE06 results, we additionally evaluated an HSE06 (001) STO—LSF slab with one La at the interface and an LSF oxygen stoichiometry of $La_{0.5}Sr_{0.5}FeO_{2.875}$, chosen to closely resemble the (110) slab used in the main text. This (001) slab yields a VBM offset of 0.95 eV, consistent with the 1.0 eV obtained from the (110) geometry, supporting that minimizing interfacial dipoles leads to a robust band alignment.

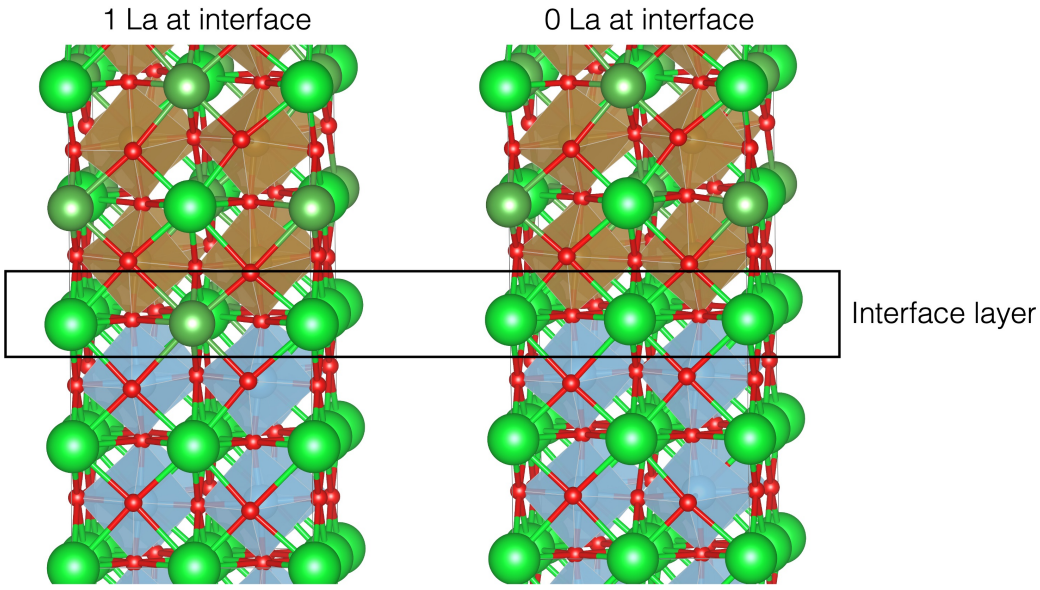

Figure 5. Slab structures for (001) interfaces between STO and LSF.

S.I.6: Interface slab structures

Fig. 6 summarizes the interface slab geometries used to align band energies. STO is (110) oriented in all slabs. STO|LSF is a coherent (110)|(110) perovskite-perovskite interface whereas STO|LMO uses LMO in the (110) orientation and STO|CeO_2 uses CeO_2 in the (111) orientation. These choices yield fully stoichiometric slabs with bulk-like compositions in the interior regions used for core-level alignment. In the perovskite slab, octahedral tilting is strongly different in STO vs. LSF. For STO|LMO and STO|CeO_2, interfacial distortion/tilting is observed, but the perovskite-like regions away from the interface remain well relaxed, consistent with the close agreement of the STO DOS in slab and bulk comparisons (S.I.9).

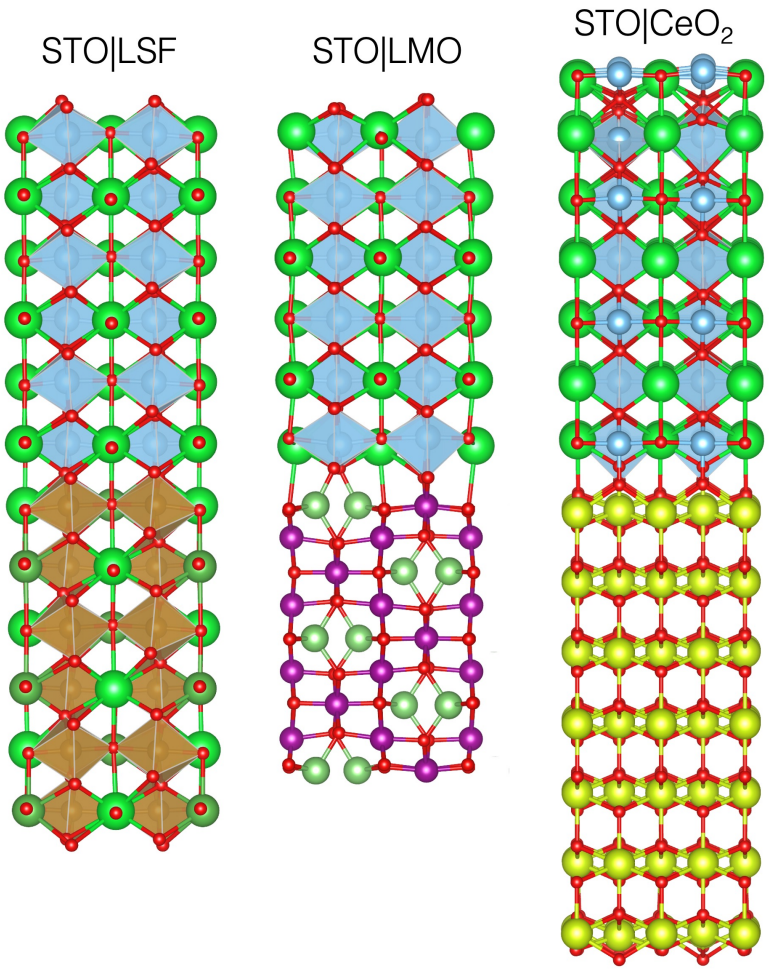

Figure 6. Slab structures for interfaces between STO and LSF, LMO, and CeO_2, from left to right

S.I.7: Impact of cell size variation on defect formation energies

Octahedral tilting in perovskites generally requires using 2nx2nx2n supercells, making 2×2×2 and 4×4×4 the only practical choices. Because this work relies on computationally expensive hybrid-functional alignment and vacancy energetics, we used 2×2×2 supercells throughout employing finite-size corrections. To give an estimate on the effect of this choice, we calculated charged vacancy formation energies with the PBE functional for STO and LSF in both a 2x2x2 and a 4x4x4 supercell. The vacancy–vacancy image distances are 8 Å and 16 Å, respectively. After applying charge and potential alignment corrections in both cases, the charged-vacancy formation energy decreases by 0.23 eV (STO) and by 0.19 eV (LSF) when increasing the supercell size. We suspect that, while the absolute value of defect formation energies might be slightly overestimated, this effect may be similar across the materials that we study here because of the almost constant cell size. We therefore estimate a residual finite-size uncertainty of $\sim$0.2 eV in absolute formation energies and in the derived $\Delta\mu_{V_O^{\cdot\cdot}}$ of different materials in this study. Given the $\sim$4 eV range spanned in this study, we accept this uncertainty to keep the computational cost tractable.

S.I.8: List of used dielectric constants

The employed electrostatic image-charge corrections according to Makov and Payne[19] require the dielectric constant of the host material. Because ionic relaxation is allowed for defective structures, we use the static dielectric constant ε_0 (electronic + ionic contributions)[20]. Whenever possible, we use room-temperature values, as this yields by far the largest database of comparable values. Still, reported ε_0 values can show substantial scatter, both experimentally (electrode/grain-boundary contributions, frequency dependence) and computationally (functional and methodology dependence).

STO and SMO exhibit well-established and rather large static dielectric constants (330 at RT for STO[21] and 145 at RT for SMO[22]). For metallic SFO, reported dielectric constants are also high ($>$100)[23] and computed values are on the order of $\sim$70[24]. We therefore use $\varepsilon_0 = 100$, noting that the correction is only very weakly sensitive to the exact value in this high-ε_0 regime. For LCF/LSF/LBF, reliable datasets are scarce and values cluster broadly around 10–30[25–27], with a slight increase from LCF to LBF. For the undoped $LaFeO_3$, literature suggests a room temperature static dielectric constant between 20-40[28,29]. We choose $\varepsilon_0 = 15, 20$, and 25 for LCF, LSF, and LBF, respectively. For LSM, literature reports static dielectric constant values between 30-50[30,31], and we use an average value of 40 in this study. For $LiMn_2O_4$, we use a static dielectric constant of 11[32], and a value of 26 for CeO_2[33].

material	ε_0	reference
STO	330	[21]
SMO	145	[22]
SFO	100	[23, 24]
LCF	15	[25]
LSF	20	[26]
LBF	25	[27]
LSM	40	[30, 31]
$LiMn_2O_4$	11	[32]
CeO_2	26	[33]

S.I.9: Comparison of DOS from slab and bulk structures

To validate the band-alignment procedure based on interface slabs, we compare the total DOS of bulk STO with the DOS of the central STO layer extracted from four slabs (STO interfaced with SMO, SFO, LMO, and CeO_2). Differences are most pronounced in the valence-band region (Fig. 7), consistent with the valence band being more sensitive to interfacial strain and structural nonidealities than deep core levels.

After aligning all DOS to the Sr 3*s* core level, the O 2*p* centroid is 332.25±0.15 across bulk and slab-derived STO, with the largest deviations occurring for STO|LMO and STO|CeO_2, where STO experiences the largest interfacial strain. The Sr 4*p* centroid remains nearly constant at 19.38±0.05 eV. We therefore estimate that the alignment uncertainty introduced by the slab approach is ≈0.1 eV, well below most band offsets discussed in the main text.

Here, we also want to discuss possible strain effects. For bulk STO, structural relaxation yields a cubic lattice parameter of 3.91 Å, in good agreement with experiment. In pure perovskite slabs, this lattice constant varies between 3.95 Å(when interfacing LBF) and 3.90 Å(when interfacing SMO), corresponding to a maximal strain of around 1% for the central STO layer. When interfacing CeO_2, the STO lattice parameter amounts to 3.90 Å, also exhibiting minimal strain. The maximal strain is observed for the STO|LMO interface, with an STO lattice parameter of 3.96 Å, indicating rather strong tensile strain on the order of 2%. We performed test calculations of isotropically strained bulk STO with -1% and +1% strain, and found shifts of the VBM of around 0.1 eV when referenced to the Sr3s level, therefore, we suspect that strain-induced effects do not substantially alter the trends observed in this study.

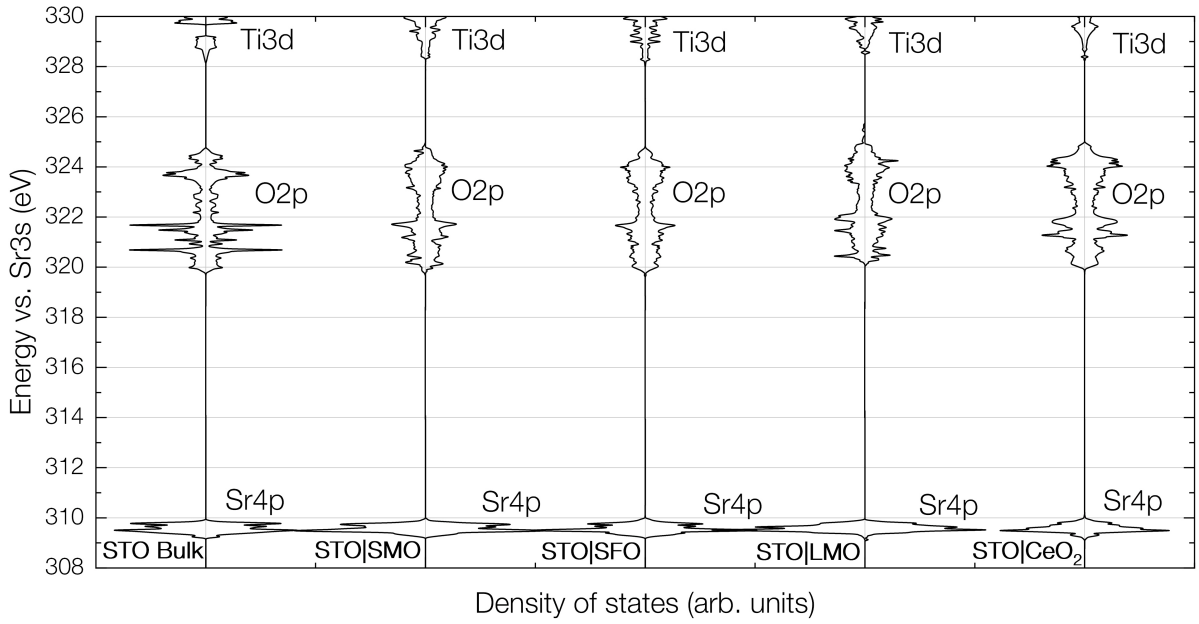

Figure 7. Total densities of states of $SrTiO_3$ from a bulk calculation and the central layer in slab structures, referenced to the Sr 3*s* core level.

S.I.10: Connecting $\mu_{h^\cdot}^0$ and $\mu_{V_O^{\cdot\cdot}}^0$ to electronic structure

Fig. 8 summarizes how the electronic structure controls the separate contributions to charged oxygen vacancy formation. First, the absolute placement of electronic levels (in particular the O $2p$ manifold) reflects the electrostatic environment of oxygen in the lattice (e.g. changes in lattice geometry and Madelung stabilization). Shifting the O $2p$ manifold upward on an absolute energy scale generally destabilizes lattice oxygen and lowers the cost of oxide ion removal, best seen in the trend between LBF and LCF. Shifting the O $2p$ states to lower energies increases the charged vacancy formation energy, e.g. in LMO.

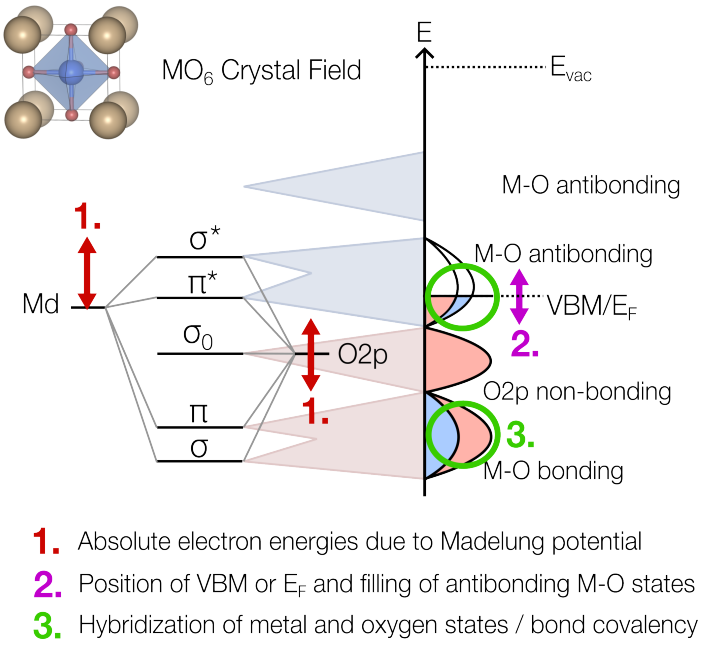

Figure 8. Schematic DOS of a perovskite oxide derived from the molecular orbital diagram of MO_6 octahedra[7]. The main levers for $\mu_{h^\cdot}^0$ and $\mu_{V_O^{\cdot\cdot}}^0$ are indicated with arrows, circles and bold numbers.

Second, the position of the electronic reservoir sets $\mu_{h^\cdot}^0$. Under hole-compensated conditions, $\mu_{h^\cdot}^0$ is linked to the position of the VBM (and, more generally, to the Fermi level under the relevant defect-chemical conditions). Changing the average oxidation state of the metal-oxygen sublattice therefore modifies the energy gain during electron redistribution even if the local lattice response remains similar. In addition, in perovskite oxides, hybridized metal-oxygen states above the nonbonding O $2p$ states are antibonding in nature, and lifting the Fermi energy also impacts the cost of oxide ion removal.

Third, metal-oxygen hybridization controls the separation and mixing of metal d and O $2p$ states and, crucially, the presence and occupation of antibonding states. In relatively ionic perovskites such as STO, the VBM is dominated by largely nonbonding O $2p$ states, whereas in covalent systems, such as SFO, the highest occupied states are of antibonding character, which destabilizes lattice oxygen and lowers the cost of oxide ion removal. This effect is not fully captured by the O $2p$ centroid alone, since the centroid does not distinguish bonding and antibonding contributions.

References

1. Linstrom, P. J. & Mallard, W. G. The NIST Chemistry WebBook: A chemical data resource on the internet. *Journal of Chemical & Engineering Data* **46,** 1059–1063. doi:10.1021/je000236i (2001).
2. Siebenhofer, M., Baiutti, F., de Dios Sirvent, J., Huber, T. M., Viernstein, A., Smetaczek, S., Herzig, C., Liedke, M. O., Butterling, M., Wagner, A., *et al.* Exploring point defects and trap states in undoped $SrTiO_3$ single crystals. *Journal of the European Ceramic Society* **42,** 1510–1521. doi:10.1016/j.jeurceramsoc.2021.10.010 (2022).
3. Schmid, A., Rupp, G. M. & Fleig, J. Voltage and partial pressure dependent defect chemistry in (La, Sr) $FeO_{3-\delta}$ thin films investigated by chemical capacitance measurements. *Physical Chemistry Chemical Physics* **20,** 12016–12026. doi:10.1039/C7CP07845E (2018).
4. Steinbach, C., Schmid, A., Siebenhofer, M., Nenning, A., Rameshan, C., Kubicek, M. & Fleig, J. Space Charges at $SrTiO_3$| Mixed Ionic and Electronic Conducting Oxide Heterojunctions and Their Relation to Defect Chemistry. *ACS Applied Materials & Interfaces* **17,** 17543–17557. doi:10.1021/acsami.4c21843 (2025).
5. Lee, Y.-L., Kleis, J., Rossmeisl, J., Shao-Horn, Y. & Morgan, D. Prediction of solid oxide fuel cell cathode activity with first-principles descriptors. *Energy & Environmental Science* **4,** 3966–3970 (2011).
6. Lee, Y.-L., Lee, D., Wang, X. R., Lee, H. N., Morgan, D. & Shao-Horn, Y. Kinetics of oxygen surface exchange on epitaxial Ruddlesden-Popper phases and correlations to first-principles descriptors. *The Journal of Physical Chemistry Letters* **7,** 244–249 (2016).
7. Hong, W. T., Risch, M., Stoerzinger, K. A., Grimaud, A., Suntivich, J. & Shao-Horn, Y. Toward the rational design of non-precious transition metal oxides for oxygen electrocatalysis. *Energy & Environmental Science* **8,** 1404–1427. doi:10.1039/C4EE03869J (2015).
8. Jacobs, R., Hwang, J., Shao-Horn, Y. & Morgan, D. Assessing correlations of perovskite catalytic performance with electronic structure descriptors. *Chemistry of Materials* **31,** 785–797. doi:10.1021/acs.chemmater.8b03840 (2019).
9. Wexler, R. B., Gautam, G. S., Stechel, E. B. & Carter, E. A. Factors Governing Oxygen Vacancy Formation in Oxide Perovskites. *Journal of the American Chemical Society* **143,** 13212–13227. doi:10.1021/jacs.1c05570 (2021).
10. Deml, A. M., Holder, A. M., O'Hayre, R. P., Musgrave, C. B. & Stevanovic, V. Intrinsic material properties dictating oxygen vacancy formation energetics in metal oxides. *The journal of physical chemistry letters* **6,** 1948–1953. doi:10.1021/acs.jpclett.5b00710 (2015).
11. Krammer, M., Schmid, D., Kubicek, M. & Fleig, J. Utilizing oxygen gas storage in rechargeable oxygen ion batteries. *Journal of Power Sources* **571,** 233167. doi:10.1016/j.jpowsour.2023.233167 (2023).
12. Kubicek, M., Bork, A. H. & Rupp, J. L. Perovskite oxides–a review on a versatile material class for solar-to-fuel conversion processes. *Journal of Materials Chemistry A* **5,** 11983–12000. doi:10.1039/C7TA00987A (2017).
13. Gregori, G., Merkle, R. & Maier, J. Ion conduction and redistribution at grain boundaries in oxide systems. *Progress in Materials Science* **89,** 252–305. doi:10.1016/j.pmatsci.2017.04.009 (2017).
14. Maier, J. Ionic Conduction in Space Charge Regions. *Progress in Solid State Chemistry* **23,** 171–263. doi:10.1016/0079-6786(95)00004-E (1995).
15. Nicollet, C., Toparli, C., Harrington, G. F., Defferriere, T., Yildiz, B. & Tuller, H. L. Acidity of surface-infiltrated binary oxides as a sensitive descriptor of oxygen exchange kinetics in mixed conducting oxides. *Nature Catalysis* **3,** 913–920. doi:10.1038/s41929-020-00520-x (2020).
16. Siebenhofer, M., Nenning, A., Rameshan, C., Blaha, P., Fleig, J. & Kubicek, M. Engineering surface dipoles on mixed conducting oxides with ultra-thin oxide decoration layers. *Nature Communications* **15,** 1730. doi:10.1038/s41467-024-45824-9 (2024).
17. Riedl, C., Siebenhofer, M., Nenning, A., Wilson, G. E., Kilner, J., Rameshan, C., Limbeck, A., Opitz, A. K., Kubicek, M. & Fleig, J. Surface Decorations on Mixed Ionic and Electronic Conductors: Effects on Surface Potential, Defects, and the Oxygen Exchange Kinetics. *ACS Applied Materials & Interfaces.* doi:10.1021/acsami.3c03952 (2023).
18. Siebenhofer, M., Grajkowski, F., Nicollet, C., Yildiz, B., Fleig, J. & Kubicek, M. Reducibility, adsorption energies, surface acidity–fundamental material properties for fast oxygen exchange. *Journal of Materials Chemistry A* **13,** 29885–29899. doi:10.1039/D5TA05637C (2025).
19. Makov, G & Payne, M. C. Periodic boundary conditions in ab initio calculations. *Physical Review B* **51,** 4014. doi:10.1103/PhysRevB.51.4014 (1995).

20. Kumagai, Y. & Oba, F. Electrostatics-based finite-size corrections for first-principles point defect calculations. *Physical Review B* **89,** 195205. doi:10.1103/PhysRevB.89.195205 (2014).

21. Neville, R. C., Hoeneisen, B. & Mead, C. Permittivity of strontium titanate. *Journal of Applied Physics* **43,** 2124–2131. doi:10.1063/1.1661463 (1972).

22. Kamba, S., Goian, V., Skoromets, V., Hejtmánek, J., Bovtun, V., Kempa, M., Borodavka, F., Vaněk, P., Belik, A., Lee, J., *et al.* Strong spin-phonon coupling in infrared and Raman spectra of $SrMnO_3$. *Physical Review B* **89,** 064308. doi:10.1103/PhysRevB.89.064308 (2014).

23. Aich, P., Fu, D., Meneghini, C. & Ray, S. Identifying the nature of dielectric anomalies in $SrFeO_{3-\delta}$. *Journal of Magnetism and Magnetic Materials* **486,** 165265. doi:10.1016/j.jmmm.2019.165265 (2019).

24. Petousis, I., Mrdjenovich, D., Ballouz, E., Liu, M., Winston, D., Chen, W., Graf, T., Schladt, T. D., Persson, K. A. & Prinz, F. B. High-throughput screening of inorganic compounds for the discovery of novel dielectric and optical materials. *Scientific data* **4,** 160134. doi:10.1038/sdata.2016.134 (2017).

25. Kashyap, S. J., Sankannavar, R. & Madhu, G. Insights on the various structural, optical and dielectric characteristics of $La_{1-x}Ca_xFeO_3$ perovskite-type oxides synthesized through solution-combustion technique. *Applied Physics A* **128,** 518. doi:10.1007/s00339-022-05628-4 (2022).

26. Huang, L., Cheng, L., Pan, S., He, Y., Tian, C., Yu, J. & Zhou, H. Effects of Sr doping on the structure, magnetic properties and microwave absorption properties of $LaFeO_3$ nanoparticles. *Ceramics International* **46,** 27352–27361. doi:10.1016/j.ceramint.2020.07.220 (2020).

27. Huang, L., Cheng, L., Pan, S., Yao, Q., Long, Q., Wang, M., Chen, Y. & Zhou, H. Influence of A-site doping barium on structure, magnetic and microwave absorption properties of $LaFeO_3$ ceramics powders. *Journal of Rare Earths* **40,** 1106–1117. doi:10.1016/j.jre.2021.05.009 (2022).

28. Ctibor, P., Sedláček, J., Illková, K. & Straka, L. Characterization of $LaFeO_3$ Dielectric Ceramics Produced by Spark Plasma Sintering. *Materials* **17,** 287. doi:10.3390/ma17020287 (2024).

29. Idrees, M, Nadeem, M, Atif, M, Siddique, M, Mehmood, M & Hassan, M. Origin of colossal dielectric response in $LaFeO_3$. *Acta Materialia* **59,** 1338–1345. doi:10.1016/j.actamat.2010.10.066 (2011).

30. Kang, M.-G. & Kang, Y.-M. Effect of Mn content on the structure, electromagnetic properties, and electromagnetic wave absorption characteristics in $La_{0.7}Sr_{0.3}Mn_{1+x}O_3$. *Ceramics International* **49,** 40043–40050. doi:10.1016/j.ceramint.2023.09.334 (2023).

31. Ivanov, V. Y., Travkin, V., Mukhin, A., Lebedev, S., Volkov, A., Pimenov, A., Loidl, A., Balbashov, A. & Mozhaev, A. Magnetic, dielectric, and transport properties of $La_{1-x}Sr_xMnO_3$ at submillimeter wavelengths. *Journal of applied physics* **83,** 7180–7182. doi:10.1063/1.367675 (1998).

32. Hoang, K. Understanding the electronic and ionic conduction and lithium over-stoichiometry in $LiMn_2O_4$ spinel. *Journal of Materials Chemistry A* **2,** 18271–18280. doi:10.1039/C4TA04116J (2014).

33. Tye, L, El-Masry, N., Chikyow, T, McLarty, P & Bedair, S. Electrical characteristics of epitaxial CeO_2 on Si (111). *Applied physics letters* **65,** 3081–3083. doi:10.1063/1.112467 (1994).